Appl. Phys. B 84, 11–18 (2006)
DOI: 10.1007/s00340-006-2218-x

Applied Physics B
Lasers and Optics

K.L. SHUFORD[1]
M.A. RATNER[1]
S.K. GRAY[2]
G.C. SCHATZ[1,✉]

Finite-difference time-domain studies of light transmission through nanohole structures

[1] Department of Chemistry, Northwestern University, 2145 Sheridan Road, Evanston, IL 60208-3113, USA
[2] Chemistry Division, Argonne National Laboratory, Argonne, IL 60439, USA

Received: 15 December 2005/Revised version: 17 March 2006
Published online: 22 April 2006 •

ABSTRACT We present theoretical studies on the transmission of light through subwavelength, circular apertures surrounded by circular groove structures. Finite-difference time-domain equations in cylindrical coordinates are provided for both dispersive materials and electrical conductors. The nanohole systems are composed of a circular hole in a slab, that is encircled by sinusoidal grooves defined by a period and depth. Light transmission is found to be extremely sensitive to the hole size, groove period, and groove depth. We determine a set of groove parameters that optimize transmission. Enhancements in transmission by approximately a factor of four can be achieved for silver in the visible when compared to the light incident upon the hole. These results may find utility in the design of nanoscale light manipulating devices.

PACS 73.20.Mf; 78.20.Ci; 78.68.+m; 64.47.-n; 03.50.De

1 Introduction

There has been renewed interest in recent years in the interaction of light with subwavelength apertures due to the experimental finding that hole arrays can transmit more radiation than is expected from geometric optics [1]. Also, the transmission far exceeds the $(D/\lambda)^4$ dependence (D is the hole diameter, λ is incident wavelength) predicted for a hole in an infinitely thin conductor [2]. The use of materials that support plasmon excitation has been proposed as the primary source of the large transmission enhancements [3]. It has also been shown that patterning the metallic surface further enhances transmission, as well as significantly reducing the divergence of light on the exit side of the slab [4]. These findings are particularly intriguing from an applications perspective. The manipulation of light on the nanoscale has numerous applications such as optical filters, focusing devices, fabrication techniques, and near-field optical technologies.

The majority of studies on holes have been performed on two-dimensional square arrays. Both experiment [1, 5, 6] and theory [7–9] show multiple peaks in the transmission spectra as a result of the lattice periodicity. Array structures that are closely spaced produce a coupling between holes due to propagating plasmon effects. Single apertures eliminate the interhole coupling, and can provide valuable information on a more fundamental level regarding transmission characteristics and mechanisms.

Theoretical studies of single nanoholes have been primarily concerned with the effect of the aperture on transmission properties. The transmission enhancements from single nanoholes in flat surfaces are typically modest when compared to the predictions of geometric optics [10, 11]. The addition of periodic grooves can greatly enhance transmission, and it also changes the angular distribution of the transmitted light [12]. Similar findings have been reported for subwavelength slits surrounded by grooves [4, 13–15]. Baida et al. [12] have investigated the effects produced by varying the shape of the holes, but did not emphasize the patterned surface. Our intent has been to complement their studies by exploring systems with a constant aperture shape and altering the surface structure.

In this manuscript, we investigate the transmission through a single, subwavelength nanohole surrounded by concentric grooves. Focus has been put not only on the effects produced by changing the hole and slab sizes, but also on the transmission enhancements that can be gained by optimizing the grating characteristics. Our results allow general statements to be made regarding the contributions to, and mechanism for transmission, as well as provide a blueprint for how to design structures that yield the largest enhancements.

2 Theory

We investigate the optical properties of nanohole systems using the finite-difference time-domain method (FDTD) [16]. The FDTD method is a time marching algorithm, which solves Maxwell's curl equations on a numeric grid. A propagation yields the temporal evolution of both the electric and magnetic fields at every point in space. In the most common formulations based on the Yee algorithm [17], the grid is evenly spaced, yet staggered. That is to say, the electric and magnetic field components are evaluated at half-step intervals from one another temporally and spatially. This grid arrangement produces central-difference equations that are second-order accurate in both time and space [16].

The materials of interest are linear, isotropic, and dispersive. The frequency dependence of the electric properties is

✉ Fax: +1-847-491-7713, E-mail: schatz@chem.northwestern.edu

included through a Drude representation for the permittivity of the metal. This formulation incorporates the metallic dispersion via an additional differential equation that is propagated simultaneously with the electric and magnetic fields (see Appendix A). Maxwell's equations under these conditions can be written as

$$\frac{\partial \boldsymbol{H}}{\partial t} = -\frac{1}{\mu_0}\nabla \times \boldsymbol{E} \tag{1}$$

$$\frac{\partial \boldsymbol{E}}{\partial t} = \frac{1}{\varepsilon_{\text{eff}}}\left(\nabla \times \boldsymbol{H} - \boldsymbol{J}\right) \tag{2}$$

$$\frac{\partial \boldsymbol{J}}{\partial t} = \varepsilon_0 \omega_{\text{p}}^2 \boldsymbol{E} - \gamma \boldsymbol{J} \tag{3}$$

where $\boldsymbol{H}$, $\boldsymbol{E}$, $\boldsymbol{J}$, μ_0, and ε_0, are the magnetic field, electric field, current density, permeability of free space, and permittivity of free space respectively.

All of the vectors in (1)–(3) are functions of time and space, while the permeability and permittivity terms have a spatial dependence through the material defined at each grid point. If the grid location is designated as a vacuum site, $\boldsymbol{J}$ is required to remain zero (the current density is set to zero initially), and $\varepsilon_{\text{eff}} = \varepsilon_0$. If the grid point is designated as metallic, $\varepsilon_{\text{eff}} = \varepsilon_0 \varepsilon_\infty$, and the Drude parameters are included to represent the dispersive properties. As in [18], the parameters are fit to match experimental permittivity data for silver [19] over the wavelength range of interest. We are interested here in the 400–800 nanometer (nm) range, and find that $\varepsilon_\infty = 4.1683$, $\omega_{\text{p}} = 8.8335$ eV, and $\gamma = 0.14015$ eV yield a good description of both the real and imaginary parts of the permittivity.

The systems of interest are metallic films with a single hole surrounded by concentric grooves. This geometry is most conveniently treated in cylindrical coordinates, where the vectors have ϱ, φ, and z components. The nanohole system has axial symmetry, making the field components periodic in the azimuthal direction. As a result of this, the φ dependence can be included via Fourier series expansion. In general, the number of terms needed in the expansion depends on the orientation of the system with respect to the incident field. For the case of a normal incident wave, only the first term in the expansion is needed [20]. We will limit our treatment to this case, where the incident field is propagating in z and polarized in the x–y plane. This assumption eliminates the angular dependence in the problem, and reduces the spatial grid from three to two dimensions. Note that there are still six field components to propagate even though the grid dimension has been reduced.

As mentioned earlier, the electric and magnetic field components are staggered by half-step increments in both time and space. The lattice points are represented by indices i and j, where $\varrho = i\Delta\varrho$ and $z = j\Delta z$. The label n indicates the time step such that the $\boldsymbol{E}$ field components are evaluated at $t = (n+0.5)\Delta t$, while the $\boldsymbol{H}$ field components are evaluated at $t = n\Delta t$. The FDTD expressions for the components are then

$$\begin{aligned}\boldsymbol{H}_\varrho^n(i,j) = \boldsymbol{H}_\varrho^{n-1}(i,j) &+ \frac{\Delta t}{\mu_0 \varrho_0(i)} \boldsymbol{E}_z^{n-0.5}(i,j) \\ &+ \frac{\Delta t}{\mu_0 \Delta z}\left[\boldsymbol{E}_\varphi^{n-0.5}(i,j+1) - \boldsymbol{E}_\varphi^{n-0.5}(i,j)\right]\end{aligned} \tag{4}$$

$$\begin{aligned}\boldsymbol{H}_\varphi^n(i,j) = \boldsymbol{H}_\varphi^{n-1}(i,j) &- \frac{\Delta t}{\mu_0 \Delta z} \\ &\times \left[\boldsymbol{E}_\varrho^{n-0.5}(i,j+1) - \boldsymbol{E}_\varrho^{n-0.5}(i,j)\right] \\ &+ \frac{\Delta t}{\mu_0 \Delta \varrho}\left[\boldsymbol{E}_z^{n-0.5}(i+1,j) - \boldsymbol{E}_z^{n-0.5}(i,j)\right]\end{aligned} \tag{5}$$

$$\begin{aligned}\boldsymbol{H}_z^n(i,j) = \boldsymbol{H}_z^{n-1}(i,j) &- \frac{\Delta t}{\mu_0 \varrho(i)} \boldsymbol{E}_\varrho^{n-0.5}(i,j) - \frac{\Delta t}{\mu_0 \varrho(i) \Delta \varrho} \\ &\times \left[\varrho_0(i+1)\boldsymbol{E}_\varphi^{n-0.5}(i+1,j) - \varrho_0(i)\boldsymbol{E}_\varphi^{n-0.5}(i,j)\right]\end{aligned} \tag{6}$$

$$\begin{aligned}\boldsymbol{E}_\varrho^{n+0.5}(i,j) = \boldsymbol{E}_\varrho^{n-0.5}(i,j) &+ \frac{\Delta t}{\varepsilon_{\text{eff}} \varrho(i)} \boldsymbol{H}_z^n(i,j) \\ &- \frac{\Delta t}{\varepsilon_{\text{eff}} \Delta z}\left[\boldsymbol{H}_\varphi^n(i,j) - \boldsymbol{H}_\varphi^n(i,j-1)\right] \\ &- \frac{\Delta t}{\varepsilon_{\text{eff}}} \boldsymbol{J}_\varrho^n(i,j)\end{aligned} \tag{7}$$

$$\begin{aligned}\boldsymbol{E}_\varphi^{n+0.5}(i,j) = \boldsymbol{E}_\varphi^{n-0.5}(i,j) &+ \frac{\Delta t}{\varepsilon_{\text{eff}} \Delta z}\left[\boldsymbol{H}_\varrho^n(i,j) - \boldsymbol{H}_\varrho^n(i,j-1)\right] \\ &- \frac{\Delta t}{\varepsilon_{\text{eff}} \Delta \varrho}\left[\boldsymbol{H}_z^n(i,j) - \boldsymbol{H}_z^n(i-1,j)\right] \\ &- \frac{\Delta t}{\varepsilon_{\text{eff}}} \boldsymbol{J}_\varphi^n(i,j)\end{aligned} \tag{8}$$

$$\begin{aligned}\boldsymbol{E}_z^{n+0.5}(i,j) = \boldsymbol{E}_z^{n-0.5}(i,j) &- \frac{\Delta t}{\varepsilon_{\text{eff}} \varrho_0(i)} \boldsymbol{H}_\varrho^n(i,j) - \frac{\Delta t}{\varepsilon_{\text{eff}}} \boldsymbol{J}_z^n(i,j) \\ &+ \frac{\Delta t}{\varepsilon_{\text{eff}} \varrho_0(i) \Delta \varrho} \\ &\times \left[\varrho(i)\boldsymbol{H}_\varphi^n(i,j) - \varrho(i-1)\boldsymbol{H}_\varphi^n(i-1,j)\right]\end{aligned} \tag{9}$$

$$\begin{aligned}\boldsymbol{J}_\chi^n(i,j) = &\frac{\left(1 - \frac{\gamma \Delta t}{2}\right)}{\left(1 + \frac{\gamma \Delta t}{2}\right)} \boldsymbol{J}_\chi^{n-1}(i,j) \\ &+ \frac{\Delta t\, \varepsilon_0\, \omega_{\text{p}}^2}{\left(1 + \frac{\gamma \Delta t}{2}\right)} \boldsymbol{E}_\chi^{n-0.5}(i,j) \qquad \chi = \varrho, \varphi, z,\end{aligned} \tag{10}$$

where $\varrho_0(i) = (i-1)\Delta\varrho$ and $\varrho(i) = (i-0.5)\Delta\varrho$ are the radii associated with the left side and the center of the block respectively. The more complex coefficients present in (10) are the result of placing the current density components on a suitable time grid to be added to the magnetic field components [21].

Transmission is found by calculating the flux of the electromagnetic energy through a bounding surface in the forward hemisphere, and normalizing with the appropriate incident flux. The frequency resolved, total fields are obtained by discrete Fourier transformation of the time domain fields

$$\boldsymbol{E}(\omega) = \int_0^T \mathrm{d}t \exp(i\omega t)\boldsymbol{E}(t) \tag{11}$$

$$\boldsymbol{H}(\omega) = \int_0^T \mathrm{d}t \exp(i\omega t)\boldsymbol{H}(t), \tag{12}$$

and are explicitly calculated on the bounding surface. All of the fields have been propagated for 5 fs ($T = 5.0 \times 10^{-15}$ s) using a 1.67 as (1.67×10^{-18} s) time step. The time-averaged Poynting vector [18, 22] is

$$\boldsymbol{S}(\omega) = \frac{1}{2}\,\mathrm{Re}\left\{\boldsymbol{E}(\omega) \times \boldsymbol{H}^{*}(\omega)\right\}, \tag{13}$$

which specifies the magnitude and direction of electromagnetic energy in the frequency domain. The net rate electromagnetic energy is transferred through a bounding surface (energy flux) is

$$W = \int_{A} \mathrm{d}A\,\boldsymbol{S}(\omega) \cdot \hat{n}\,, \tag{14}$$

where $\hat{n}$ is the outward unit vector perpendicular to surface A. We define the transmission as the ratio of (14) to the equivalent expression using the incident fields. Note that the surface integrals should only be evaluated in the forward direction to correspond to transmission. The incident flux can be calculated analytically for a plane wave; however, we choose to propagate the fields using the FDTD algorithm in the absence of the metal slab to keep the calculated rates on equal footing. For aperture structures, it is convenient to normalize the transmission in an alternative way to better connect with geometric optics. We define a normalized transmission as

$$T_{\mathrm{norm}} = \frac{W - W_{\mathrm{slab}}}{W_0'} \tag{15}$$

where W describes the transmission rate of the nanohole system, W_{slab} describes an identical system without a hole present, and W_0' is the incident flux integrated only over the area of the hole. This expression is meant to emphasize the effects produced from the hole by subtracting off the energy flux through a solid slab. A normalized transmission of ~ 1 indicates a result similar to that of geometric optics, and will typically occur when the hole is significantly larger than the wavelength of light.

All calculations reported have been performed using a 2200×2200 grid, where the grid size corresponds to a resolution of 1 nm. The fields have been damped at the grid boundaries to eliminate spurious reflections. This has been accomplished using a simple exponential damping technique that is common in wave packet calculations, and has proven effective for previous calculations using the FDTD method [18]. Note that there are more sophisticated approaches to absorption as outlined in [16], which should be used if it is desired to keep the computational grid as small as possible. A total field/scattered field formulation has been implemented to represent the initial excitation of the system by a plane wave [16]. This form of system excitation has been shown to be stable and effective for many different applications using the FDTD method. A near to far field transformation of the fields is not necessary for this work because light transmission is a near field effect. In these calculations, the bounding surface has been placed far enough away from the slab so as not to be affected by the evanescent fields. Note that for slit-like apertures, the near field transmission and far field transmission are equal [23], so the transmission of light through nanoholes should be affected very little by the placement of the bounding surface.

3 Results and discussion

It is well known that when light travels between materials with different refractive indices, reflection and refraction occur at the interfaces. In the simplest cases, such as a single interface or flat slab, the amount of light that is transmitted can be calculated exactly [22]. Figure 1 shows the transmission through a silver slab at normal incidence. These results are based on analytical theory and experimental dielectric constants. As expected, light transmission decreases exponentially with slab thickness. The wavelength of maximum transmission is 317 nm, corresponding to the bulk plasmon wavelength for our choice of dielectric constant [24]. A 50 nm slab transmits 42% of the incident light, while a 300 nm slab (not shown in figure) transmits less than 0.3%. There is essentially no light transmission through thick, silver slabs for wavelengths greater than 400 nm. The spectrum shows no structure at longer wavelengths. The inset of Fig. 1 displays transmission at wavelengths longer than the interband transition region (the spectral region we are primarily concerned with here) calculated using the analytic theory and the FDTD formalism outlined in Sect. 2. The excellent agreement validates our method of calculating transmission, and shows that the parameters chosen for the Drude function accurately describe the true optical properties of silver in this wavelength regime.

Figure 2 shows the effect of adding a hole into a 150 nm metal film without grooves. Panel a displays the results for a perfect electrical conductor (PEC, see Appendix B), while Panel b shows the same calculations for a silver slab. For Panel a, we see that a hole with a 50 nm radius transmits essentially no light for wavelengths longer than 400 nm, as is expected for an aperture that is much smaller than the wavelength of light. In contrast, a 400 nm diameter hole (200 nm

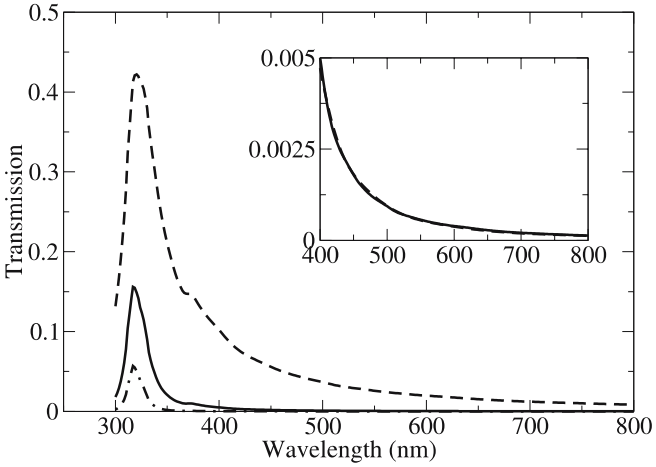

FIGURE 1 Transmission spectrum of silver slabs of varying thickness. The thicknesses are 50 nm (dashed line), 100 nm (*solid line*), and 150 nm (*dot-dashed line*), respectively. The *inset* shows the transmission of a 100 nm thick, silver slab using analytic theory (*solid line*) and the FDTD method (*dashed line*). Note that the results are nearly identical, and the two traces cannot be resolved in the figure

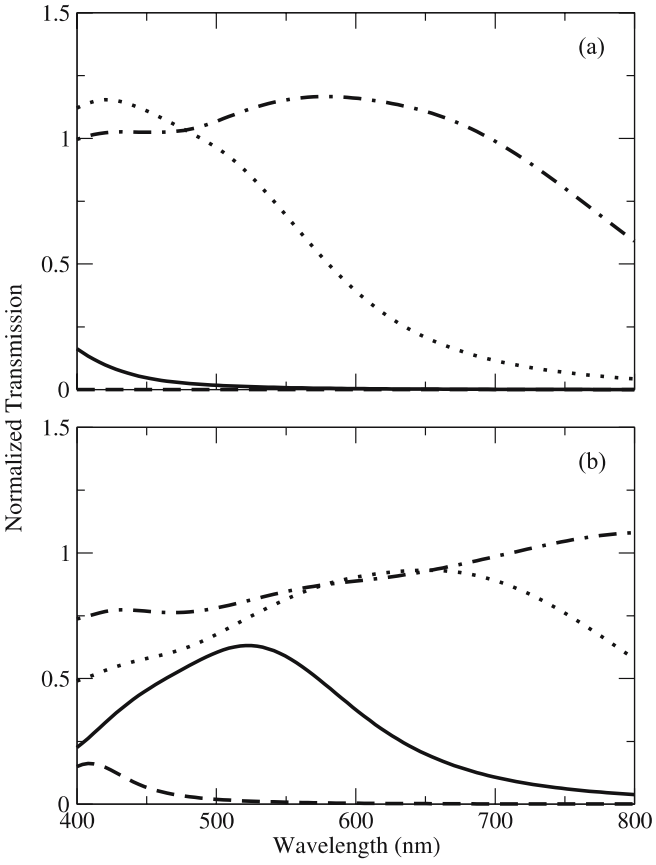

FIGURE 2 Normalized transmission of smooth slabs as a function of hole size. In *both panels*, the slab thickness is 150 nm, and hole radii are 50 nm (*dashed line*), 100 nm (*solid line*), 150 nm (*dotted line*), and 200 nm (*dot-dashed line*). *Panel a* displays results for a perfect electrical conductor, and *Panel b* shows the transmission through silver slabs

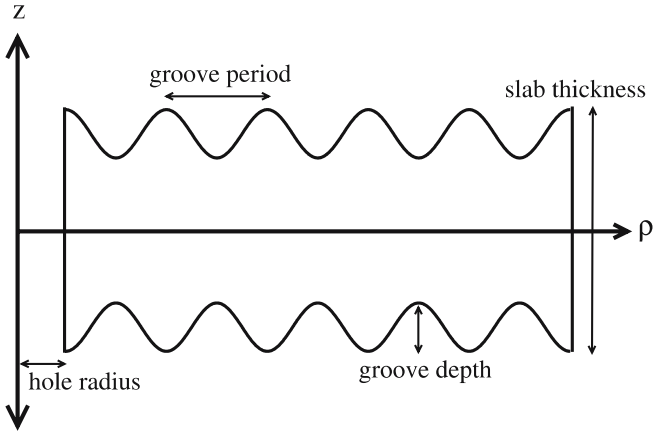

FIGURE 3 Schematic figure of the nanohole system. This is a cross section of the structure in the cylindrical coordinate grid

radius) transmits almost all of the light incident upon the hole at 400 nm, and approximately 60% of the light at 800 nm. These results are consistent with a geometric optics interpretation which states that almost all of the light is transmitted for holes similar to or larger than the wavelength, but very little is transmitted when the hole is smaller than the wavelength.

Panel b shows that the transmission peaks are red shifted when compared to the corresponding results in Panel a. The most striking difference is that for radii of 50 nm and 100 nm, the transmission spectra show significant enhancements compared to the PEC material at 405 and 520 nm, respectively. This behavior is a lot like the extinction maxima that one finds for silver nanoparticles of the same size and shape. For example, increasing the radius of the hole in a film of fixed thickness is similar to increasing the aspect ratio ($2r$/height) of a disk-shaped nanoparticle, and this leads to red shifts in extinction spectra when the polarization is perpendicular to the symmetry axis. This nanoparticle analogy reflects the importance of localized surface plasmon (LSP) excitation in the transmission through small holes. When the particles get larger (> 100 nm), the extinction peaks broaden and decrease in relative intensity, which is an effect seen in the transmission data in the form of broader "washed-out" peaks. In addition, these results are in agreement with the trends observed in transmission peaks corresponding to the first intracavity Fabry–Pérot-like resonance in metallic slit apertures upon varying the aperture size and screen thickness [25].

Previously it was noted that outgoing wave surface plasmon polaritons (SPPs) can be excited by a hole in a thin gold film [26]. Since these SPPs decay nonradiatively as they propagate on the flat film (i.e., they cannot radiate), this leads to a broadening of the hole resonances compared to the corresponding particle resonances. However, the patterning of the slab with grooves can provide the roughness needed to yield transmission that is enhanced by SPP excitation. To study this we have chosen to use sinusoidal grooves on both sides of the slab, characterized by a groove period and groove depth. The groove amplitude is at a maximum at the edge of the hole, and then oscillates over the entire slab (unless otherwise noted) as can be seen in Fig. 3. This is similar to what Lezec et al. [4] have called a "bull's eye" structure, except for minor differences in the groove shape. We obtain transmission results in very good agreement with their experimental findings when using the same grating characteristics.

Figure 4 shows the effect on transmission when the period of the grooves is varied and the hole radius is constant. Panel a displays the results for a 150 nm slab with groove depths that are 10% of the groove period. The addition of grooves alters the transmission when compared to the flat slabs regardless of period. In particular, note that groove periods of 200, 400 and 600 nm lead to peaks at 430, 460 and 600 nm, respectively. Some of the transmission enhancement at wavelengths near 650 nm is likely a result of the LSP of the hole. Recall that the grooveless structure with a 150 nm hole (Fig. 2, Panel b, dotted line) produced a broad transmission maximum close to unity at around 650 nm. The transmission enhancement from SPP excitation varies depending on the periodic structure on the surface, which defines the resonance frequency of the propagating plasmon. The results in Fig. 4 show the most significant transmission enhancements when the groove period is similar to the wavelength of the incident field, and also occurs close to the grooveless hole resonance wavelength (around 650 nm). Even when the groove period is different from the LSP wavelength, it determines the wavelength of the dominant contribution to the enhanced transmission, so the peak for a period of 400 nm is close to 400 nm. However, the

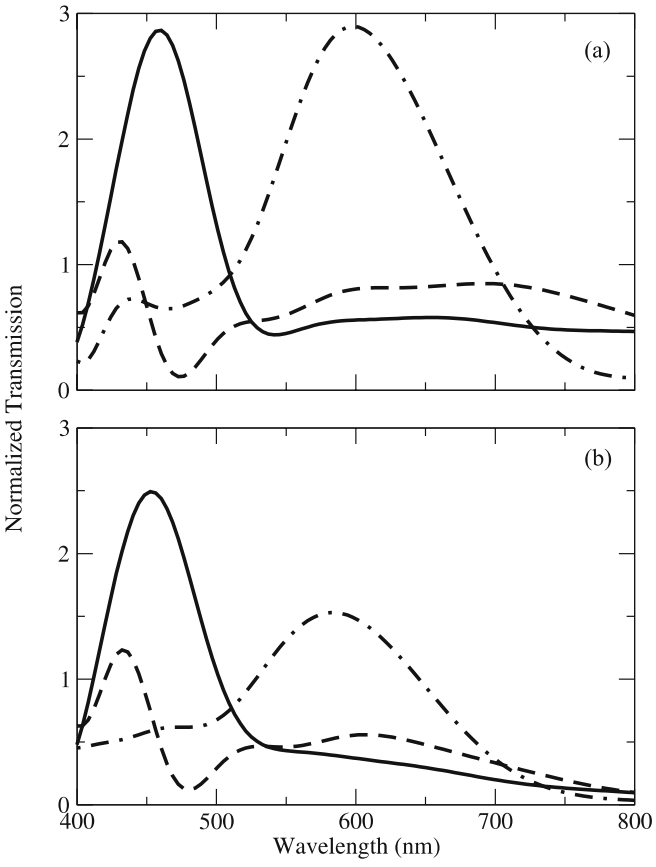

FIGURE 4 Normalized transmission of silver nanohole system as a function of groove period. In *both panels*, the hole radius is 150 nm, and the groove periods are 200 nm (*dashed line*), 400 nm (*solid line*), and 600 nm (*dot-dashed line*). The groove depth is 10% of the groove period in all traces. *Panel a* displays results for a 150 nm thick slab, and *Panel b* shows the transmission through a 300 nm thick slab

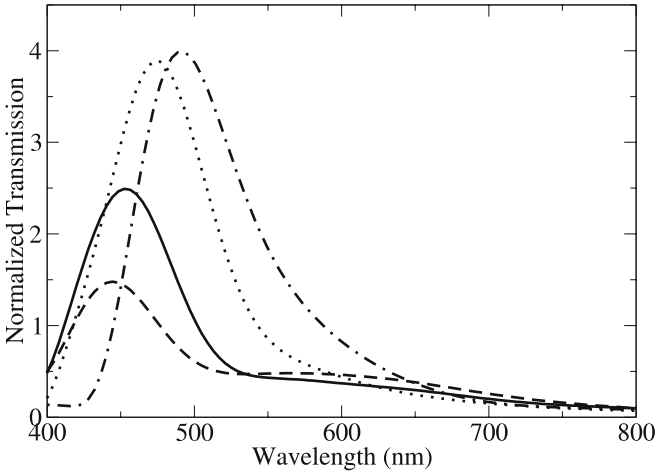

FIGURE 5 Normalized transmission of silver nanohole systems as a function of groove depth. The slab thickness is 300 nm, the hole radius is 150 nm, and the groove period is 400 nm. The groove depths are 20 nm (*dashed line*), 40 nm (*solid line*), 80 nm (*dotted line*), and 120 nm (*dot-dashed line*). Note that these depths correspond to 5%, 10%, 20%, and 30% of the groove period respectively

200 nm groove period cannot be resonant for the wavelengths considered, so we see a more complicated pattern.

Figure 4b displays the transmission produced using an identical set of groove parameters, and doubling the slab thickness to 300 nm. The major differences between panels a and b occur at wavelengths greater than 550 nm. There is little change in the location of the transmission maxima; however, the amount of transmission decreases for longer periods. The effect is most noticeable for the 600 nm period, where the transmission decreases by half. This is a result of transmission through the thin portions of the slab in the grooved structure. When the slab thickness is increased, very little light passes through these sections, yielding a significantly smaller transmission.

The calculation on the thick slab clarifies several points. In order to direct light exclusively through an aperture, the slab must be sufficiently thick. Under these conditions, it is still possible to achieve significant enhancements as is shown for the 400 nm period. The periodicity of the grooves dictates the transmission maxima, as is evident by the constant placement of these peaks upon increasing the slab thickness. This also suggests that these peaks can be attributed to SPP excitation when the groove period matches the resonant wavelength. Slight blue shifts in the broad peaks for the 200 nm and 400 nm periods are observed with increasing the slab thickness. This is again consistent with a nanoparticle analogy. Increasing the slab thickness is similar to decreasing the aspect ratio of a disk shaped nanoparticle, which would induce blue shifts in the extinction spectrum. This shows that the plasmonic properties of the metal provide the primary contributions to the enhancements in agreement with experiment [3]. We also performed calculations on PEC materials and obtained enhancements of approximately 1.5 with the transmission spectra displaying similar trends.

Changing the groove depth also affects the transmission characteristics of the system as can be seen in Fig. 5. In this figure, the slab thickness (measured from the top of the grooves) is 300 nm and the period of the grooves is 400 nm. The groove depth is varied from 5%–30% of the groove period. We have limited the groove depths to values that do not support significant transmission through the slab itself (excluding the 30% case). A groove depth corresponding to 20% of the groove period produces the maximum transmission, while still forcing the light primarily through the hole, and not compromising the mechanism of transmission. Figure 5 shows that as groove depth is increased, the transmission peak is red-shifted, broadened and increases in intensity. However once the depth is beyond a certain value, the transmission decreases and the peaks broaden.

The transmission has been calculated for a series of structures (not shown) with different depths, periods, and thicknesses. The results show that the optimal groove depth is $\sim$ 15%–20% of the groove period. Deeper grooves can transmit more light at the expense of significantly altering the transmission spectrum either by direct transmission through the slab or interference effects. In some results the peaks shifted considerably and changed shape dramatically. The effect again has to do with changing the natural frequency of the system. Both groove period and groove depth affect the frequency, but as long as the depth is kept below 20%, the period is the major contributor.

In all of the previous plots, the grooves extend the entire length of the slab. Figure 6 shows the transmission character-

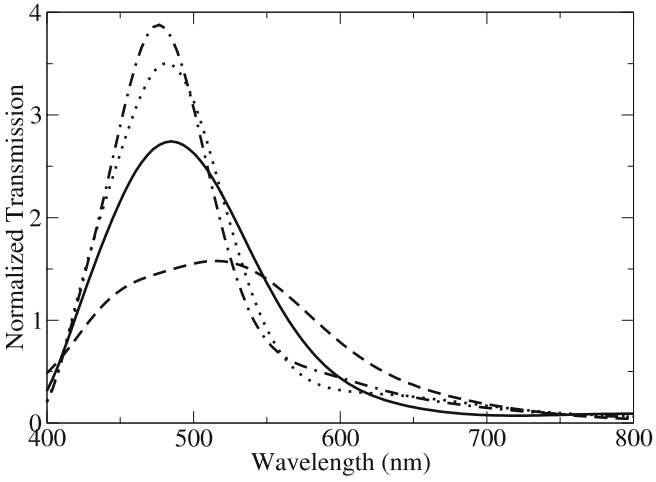

FIGURE 6 Normalized transmission of silver nanohole systems as a function of groove number. The slab thickness is 300 nm, the hole radius is 150 nm, the groove period is 400 nm, and the groove depth is 80 nm (20% of the period). The number of grooves in the slab are 1 (*dashed line*), 2 (*solid line*), 3 (*dotted line*), and 4 (*dot-dashed line*), respectively

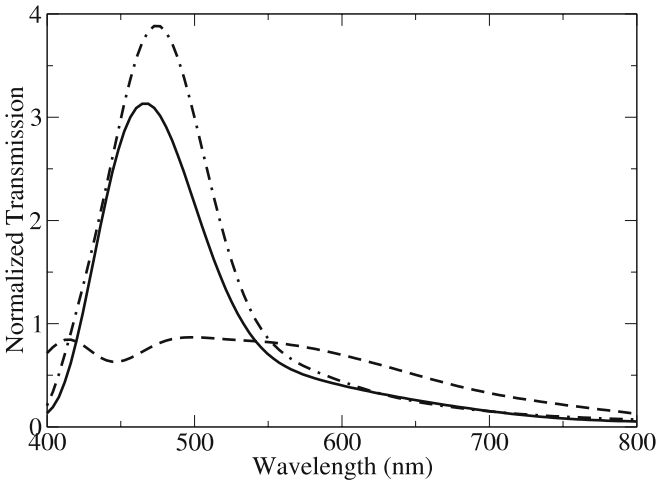

FIGURE 7 Normalized transmission of the silver nanohole system as a function of groove location. The slab thickness is 300 nm, the hole radius is 150 nm, the groove period is 400 nm, and the groove depth is 80 nm (20% of the period). The slab has grooves on the exit side (*dashed line*), entrance side (*solid line*), or both sides (*dot-dashed line*)

istics of a nanohole system as the number of grooves patterned on the slab surface is varied. For all traces in the figure, the slab thickness, hole radius, groove period, and groove depth are constant. We see that the transmission is significantly altered from that of a flat slab, even by adding a single groove. The most significant changes in the spectrum occur between the addition of the first and second grooves, where a blue shift and significant narrowing of the transmission peak is observed. The addition of grooves three and four produces a further blue shift and narrowing, but the effects are much more subtle. Adding a fifth groove affects the spectrum very little (not shown).

Similar calculations have been done on structures with different groove periods, groove depths, and slab thicknesses. The results showed that convergence is achieved in the transmission spectrum after a certain number of grooves on the slab surface; however, the number at which this occurs is different for each system. The overall length of the grooved region is a more consistent indicator of when the results will converge. We find that when the pattern extends over 1 micron (μm) the results begin to converge. Typically convergence is achieved for distances greater than 1.5 μm. These distances indicate the propagation distance of surface plasmons on the patterned silver structures. Of course, the SPP frequency is different for each system, and this leads to variation of the distance from system to system.

Another point of interest is where the grooves are located. We have performed calculations on nanohole systems with grooves present on only one side of the slab, while the other side is flat. Figure 7 shows that the majority of the transmission is a result of grooves being present on the entrance side of the hole. (The entrance side is defined as the interface that first interacts with the incident field propagating from negative infinity towards the slab.) The dashed line is the transmission produced when the surface is patterned only on the exit side. The results in this case are very similar to the transmission obtained for a nanohole system without grooves on either side, as is indicated by the flat spectrum of moderate intensity. The transmission observed when both sides of the slab have grooves is very similar to that when grooves are on the entrance side, but showing a slight increase in the peak intensity. Even though the slab is thick enough that an extremely small amount of light is directly transmitted, there is still coupling to the surface on the exit side of the slab. This result agrees with the experimental finding that patterns on the exit side actively participate in the coupling and reradiation process [4]. These results also once again demonstrate the importance of coupling to the SPP of the metal during the transmission process.

4 Conclusions

The FDTD method has been used to investigate the transmission of light through subwavelength apertures in patterned nanohole systems. The methodology has been presented in cylindrical coordinates, which is appropriate for systems with axial symmetry, and we have studied both dispersive and perfect conducting materials. We find that the transmission is extremely sensitive to the topology of the system. Altering the hole radii, groove period, groove depth, location of the grooves, and slab thickness can drastically affect the transmission spectrum. The most important transmission enhancements can be attributed to coupling to the SPP on the metal surface. For silver, enhancements in transmission of approximately a factor of four are readily observed. The best enhancements occur when the incident wavelength is similar to the period of the grooves, and the groove depth is about 20% of the groove period. The SPP decays over a distance of approximately 1.5 μm, so grooves beyond this distance are not important to the transmission of light. Lastly, most of the coupling occurs on the entrance side of the slab, with only a relatively small percentage of transmission being attributed to the patterning on the exit side. This contribution is expected to be negligible for very thick slabs.

ACKNOWLEDGEMENTS K.L.S., M.A.R., and G.C.S. thank DOE grant DEFG02-02-ER15487 and DARPA for support of this research,

and thank Anne-Sophie Louis for performing some of the preliminary calculations. S.K.G. was supported by the U.S. Department of Energy, Office of Basic Energy Sciences, Division of Chemical Sciences, Geosciences, and Biosciences under DOE contract W-31-109-ENG-38.

Appendices

Appendix A Auxiliary differential equation method

One way to introduce dispersion into the FDTD equations is to use an auxiliary differential equation (ADE) scheme [16, 18]. An additional equation is propagated along with Maxwell's equations incorporating the true dispersive properties of the metal. The simplest implementation uses a Drude function in the frequency domain to represent the relative dielectric constant

$$\varepsilon_{\mathrm{r}}(\omega) = \varepsilon_{\infty} - \frac{\omega_{\mathrm{p}}^2}{\omega^2 + i\omega\gamma}\,, \tag{A.1}$$

where ε_{∞} is the high frequency limit of the permittivity, ω_{p} is the plasma frequency, and γ is the damping constant. These three parameters are commonly fit to experimental values for a given wavelength range, and thus may make the values employed for calculations not agree with the underlying physical interpretation. Maxwell's curl expression for the magnetic field in the frequency domain is

$$\nabla \times \boldsymbol{H}(\omega) = -i\omega\varepsilon_0\varepsilon_{\mathrm{r}}(\omega)\boldsymbol{E}(\omega) \tag{A.2}$$

where the frequency dependent dielectric constant has been expanded as the relative value multiplied by the free space value. Inserting (A.1) into (A.2) yields

$$\nabla \times \boldsymbol{H}(\omega) = -i\omega\varepsilon_0\varepsilon_{\infty}\boldsymbol{E}(\omega) + \boldsymbol{J}(\omega) \tag{A.3}$$

which upon Fourier transformation to the time domain is equivalent to (2) with $\varepsilon_{\mathrm{eff}} = \varepsilon_0\varepsilon_{\infty}$. The time evolution of the current density is specified by Fourier transforming

$$\boldsymbol{J}(\omega) = i\omega\varepsilon_0\left[\frac{\omega_{\mathrm{p}}^2}{\omega^2 + i\omega\gamma}\right]\boldsymbol{E}(\omega) \tag{A.4}$$

into the time domain. This leads to

$$\frac{\partial^2\boldsymbol{J}(t)}{\partial t^2} + \gamma\frac{\partial\boldsymbol{J}(t)}{\partial t} = \varepsilon_0\omega_{\mathrm{p}}^2\frac{\partial\boldsymbol{E}(t)}{\partial t}\,, \tag{A.5}$$

which can be reduced further to the form displayed as (3). Solving (1)–(3) in the time domain is equivalent to solving Maxwell's equations in the frequency domain using (A.1) to represent the dielectric properties of the metal.

Appendix B Electrical conductor equations

The set of differential equations that describe the electrodynamics of the system are simplified when the material of interest is not dispersive. Here we address materials whose electric properties are not frequency dependent, and can be represented by a static conductivity σ. Under these conditions, Maxwell's Equations in the time domain are

$$\frac{\partial\boldsymbol{H}}{\partial t} = -\frac{1}{\mu_0}\nabla \times \boldsymbol{E} \tag{B.1}$$

$$\frac{\partial\boldsymbol{E}}{\partial t} = \frac{1}{\varepsilon_0}\left(\nabla \times \boldsymbol{H} - \sigma\boldsymbol{E}\right)\,, \tag{B.2}$$

where we have again assumed the materials are isotropic. Note that time evolution of the magnetic field is unchanged, and thus the FDTD expressions seen as (4)–(6) are still valid. However, the right hand side of (B.2) shows the subtraction of field components that are on different time grids. To remedy this, the electric field at $t = n\Delta t$ is assumed to be the average of the values at $t = (n+0.5)\Delta t$ and $t = (n-0.5)\Delta t$. Following this substitution, the FDTD expressions for the electric field components are

$$\begin{aligned}\boldsymbol{E}_{\varrho}^{n+0.5}(i,j) = {} & \frac{\left(1-\frac{\Delta t\sigma}{2\varepsilon_0}\right)}{\left(1+\frac{\Delta t\sigma}{2\varepsilon_0}\right)}\boldsymbol{E}_{\varrho}^{n-0.5}(i,j) + \frac{\left(\frac{\Delta t}{\varepsilon_0\varrho(i)}\right)}{\left(1+\frac{\Delta t\sigma}{2\varepsilon_0}\right)}\boldsymbol{H}_z^n(i,j) \\ & - \frac{\left(\frac{\Delta t}{\varepsilon_0\Delta z}\right)}{\left(1+\frac{\Delta t\sigma}{2\varepsilon_0}\right)}\left[\boldsymbol{H}_{\varphi}^n(i,j) - \boldsymbol{H}_{\varphi}^n(i,j-1)\right]\end{aligned} \tag{B.3}$$

$$\begin{aligned}\boldsymbol{E}_{\varphi}^{n+0.5}(i,j) = {} & \frac{\left(1-\frac{\Delta t\sigma}{2\varepsilon_0}\right)}{\left(1+\frac{\Delta t\sigma}{2\varepsilon_0}\right)}\boldsymbol{E}_{\varphi}^{n-0.5}(i,j) + \frac{\left(\frac{\Delta t}{\varepsilon_0\Delta z}\right)}{\left(1+\frac{\Delta t\sigma}{2\varepsilon_0}\right)} \\ & \times\left[\boldsymbol{H}_{\varrho}^n(i,j) - \boldsymbol{H}_{\varrho}^n(i,j-1)\right] \\ & - \frac{\left(\frac{\Delta t}{\varepsilon_0\Delta\varrho}\right)}{\left(1+\frac{\Delta t\sigma}{2\varepsilon_0}\right)}\left[\boldsymbol{H}_z^n(i,j) - \boldsymbol{H}_z^n(i-1,j)\right]\end{aligned} \tag{B.4}$$

$$\begin{aligned}\boldsymbol{E}_z^{n+0.5}(i,j) = {} & \frac{\left(1-\frac{\Delta t\sigma}{2\varepsilon_0}\right)}{\left(1+\frac{\Delta t\sigma}{2\varepsilon_0}\right)}\boldsymbol{E}_z^{n-0.5}(i,j) - \frac{\left(\frac{\Delta t}{\varepsilon_0\varrho_0(i)}\right)}{\left(1+\frac{\Delta t\sigma}{2\varepsilon_0}\right)}\boldsymbol{H}_{\varrho}^n(i,j) \\ & + \frac{\left(\frac{\Delta t}{\varepsilon_0\varrho_0(i)\Delta\varrho}\right)}{\left(1+\frac{\Delta t\sigma}{2\varepsilon_0}\right)} \\ & \times\left[\varrho(i)\boldsymbol{H}_{\varphi}^n(i,j) - \varrho(i-1)\boldsymbol{H}_{\varphi}^n(i-1,j)\right]\,,\end{aligned} \tag{B.5}$$

where $\varrho_0(i)$ and $\varrho(i)$ take on the values describe in Sect. 2. The semi-implicit assumption used above has been shown to be stable and accurate for all values of σ [16]. Note that for the case of an insulator $\sigma = 0$, while for a perfect electrical conductor (PEC) $\sigma = \infty$.

REFERENCES

1 T.W. Ebbesen, H.J. Lezec, H.F. Ghaemi, T. Thio, P.A. Wolff, Nature **391**, 667 (1998)
2 H.A. Bethe, Phys. Rev. **66**, 163 (1944)
3 D.E. Grupp, H.J. Lezec, T.W. Ebbesen, K.M. Pellerin, T. Thio, Appl. Phys. Lett. **77**, 1569 (2000)

4 H.J. Lezec, A. Degiron, E. Devaux, R.A. Linke, L. Martin-Moreno, F.J. Garcia-Vidal, T.W. Ebbesen, Science **297**, 820 (2002)
5 H.F. Ghaemi, T. Thio, D.E. Grupp, T.W. Ebbesen, H.J. Lezec, Phys. Rev. B **58**, 6779 (1998)
6 T. Thio, H.F. Ghaemi, H.J. Lezec, P.A. Wolff, T.W. Ebbesen, J. Opt. Soc. Am. B **16**, 1743 (1999)
7 E. Popov, M. Neviére, S. Enoch, R. Reinisch, Phys. Rev. B **62**, 16 100 (2000)
8 L. Martín-Moreno, F.J. García-Vidal, H.J. Lezec, K.M. Pellerin, T. Thio, J.B. Pendry, T.W. Ebbesen, Phys. Rev. Lett. **86**, 1114 (2001)
9 L. Salomon, F. Grillot, A.V. Zayats, F. de Fornel, Phys. Rev. Lett. **86**, 1110 (2001)
10 R. Wannemacher, Opt. Commun. **195**, 107 (2001)
11 S. Chang, S.K. Gray, G.C. Schatz, Opt. Express **13**, 3150 (2005)
12 F.I. Baida, D. Van Labeke, B. Guizal, Appl. Opt. **42**, 6811 (2003)
13 J.A. Porto, F.J. García-Vidal, J.B. Pendry, Phys. Rev. Lett. **83**, 2845 (1999)
14 F.J. García-Vidal, H.J. Lezec, T.W. Ebbesen, L. Martín-Moreno, Phys. Rev. Lett. **90**, 213 901 (2003)
15 S.S. Akarca-Biyikli, I. Bulu, E. Ozbay, Appl. Phys. Lett. **85**, 1098 (2004)
16 A. Taflove, S.C. Hagness, *Computational Electrodynamics: The Finite-Difference Time-Domain Method*, 3rd ed. (Artech House, Boston, 2005)
17 K.S. Yee, IEEE Trans. Antennas Propag. **14**, 302 (1966)
18 S.K. Gray, T. Kupka, Phys. Rev. B **68**, 45 415 (2003)
19 P.B. Johnson, R.W. Christy, Phys. Rev. B **6**, 4370 (1972)
20 D.W. Prather, S. Shi, J. Opt. Soc. Am. A **16**, 1131 (1999)
21 S.A. Cummer, IEEE Trans. Antennas Propag. **45**, 392 (1997)
22 C.F. Bohren, D.R. Huffman, *Absorption and Scattering of Light by Small Particles* (Wiley, New York, 1998)
23 S.V. Kukhlevsky, M. Mechler, L. Csapó, K. Janssens, O. Samek, Phys. Rev. B **70**, 195 428 (2004)
24 D.W. Lynch, W.R. Hunter, *Handbook of Optical Constants of Solids*, ed. by E. Palik (Academic Press, Orlando, 1985), p. 350
25 S.V. Kukhlevsky, M. Mechler, L. Csapó, K. Janssens, O. Samek, Phys. Rev. B **72**, 165 421 (2005)
26 L. Yin, V.K. Vlasko-Vlasov, A. Rydh, J. Pearson, U. Welp, S.-H. Chang, S.K. Gray, G.C. Schatz, D.B. Brown, C.W. Kimball, Appl. Phys. Lett. **85**, 467 (2004)